


## Article

# Highly Efficient and Exceptionally Durable Photooxidation Properties on $\text{Co}_3\text{O}_4/\text{g-C}_3\text{N}_4$ Surfaces

Yelin Dai <sup>1</sup>, Ziyi Feng <sup>1</sup>, Kang Zhong <sup>1</sup>, Jianfeng Tian <sup>1</sup>, Guanyu Wu <sup>1</sup>, Qing Liu <sup>2</sup>, Zhaolong Wang <sup>1</sup>, Yingjie Hua <sup>3</sup>, Jinyuan Liu <sup>1</sup>, Hui Xu <sup>1</sup> and Xingwang Zhu <sup>2,\*</sup> 

<sup>1</sup> School of the Environment and Safety Engineering, Institute for Energy Research, Jiangsu University, Zhenjiang 212013, China

<sup>2</sup> College of Environmental Science and Engineering, Yangzhou University, Yangzhou 225009, China

<sup>3</sup> The Key Laboratory of Electrochemical Energy Storage and Energy Conversion of Hainan Province, School of Chemistry and Chemical Engineering, Hainan Normal University, Haikou 571158, China

\* Correspondence: zxw@yzu.edu.cn

**Abstract:** Water pollution is a significant social issue that endangers human health. The technology for the photocatalytic degradation of organic pollutants in water can directly utilize solar energy and has a promising future. A novel  $\text{Co}_3\text{O}_4/\text{g-C}_3\text{N}_4$  type-II heterojunction material was prepared by hydrothermal and calcination strategies and used for the economical photocatalytic degradation of rhodamine B (RhB) in water. Benefitting the development of type-II heterojunction structure, the separation and transfer of photogenerated electrons and holes in 5%  $\text{Co}_3\text{O}_4/\text{g-C}_3\text{N}_4$  photocatalyst was accelerated, leading to a degradation rate 5.8 times higher than that of pure  $\text{g-C}_3\text{N}_4$ . The radical capturing experiments and ESR spectra indicated that the main active species are  $\bullet\text{O}_2^-$  and  $\text{h}^+$ . This work will provide possible routes for exploring catalysts with potential for photocatalytic applications.

**Keywords:** photocatalyst; type-II heterojunction; carrier separation; photodegradation



**Citation:** Dai, Y.; Feng, Z.; Zhong, K.; Tian, J.; Wu, G.; Liu, Q.; Wang, Z.; Hua, Y.; Liu, J.; Xu, H.; et al. Highly Efficient and Exceptionally Durable Photooxidation Properties on  $\text{Co}_3\text{O}_4/\text{g-C}_3\text{N}_4$  Surfaces. *Materials* **2023**, *16*, 3879. <https://doi.org/10.3390/ma16103879>

Academic Editor: Juan M. Coronado

Received: 23 March 2023

Revised: 22 April 2023

Accepted: 26 April 2023

Published: 22 May 2023



**Copyright:** © 2023 by the authors. Licensee MDPI, Basel, Switzerland. This article is an open access article distributed under the terms and conditions of the Creative Commons Attribution (CC BY) license (<https://creativecommons.org/licenses/by/4.0/>).

## 1. Introduction

It is well known that the situation regarding water resources is linked to environmental, social, and economic risks [1,2]. However, large volumes of wastewater dyes and pharmaceutical effluents, including methylene blue, rhodamine B, tetracycline, ciprofloxacin, and so on, have been detected in our daily water bodies [3,4]. As a result, the environmental crisis over water has become one of the top risks facing the world today. Since these pollutants have become a serious threat to humans and ecosystems, there is an urgent need to clean up these colored organic dye pollutants [5]. In order to more effectively mitigate the ecological risks brought by water environment problems, environment-friendly technical methods such as adsorption, electrochemical, and photochemical methods have been proposed. The implementation of these technologies could effectively achieve the effect of purifying wastewater. Among the many technologies, photocatalysis, as a harmless technology for substance conversion, plays an important role in the field of toxic substances conversion. However, as the core of photocatalysis technology, semiconductor photocatalysts are usually limited to green, stable materials that meet the needs of industrial use [6]. To date, several types of semiconductors, such as oxides ( $\text{TiO}_2$  [7],  $\text{ZnO}$  [8]), nitrides ( $\text{Ta}_3\text{N}_5$  [9],  $\text{C}_3\text{N}_4$  [10–14]), and sulfides ( $\text{MoS}_2$  [15,16],  $\text{CdS}$  [17,18]) have been developed. In general, as a representative semiconductor material in p-type semiconductors,  $\text{Co}_3\text{O}_4$  is highly sought after by researchers because of its excellent catalytic activity and stability in the field of photocatalysis and its high economic benefits [19–22]. However, even so, its inherent defects still greatly limit the market expansion and application of such materials, such as their low electron–hole separation rate and relatively limited optical absorption range [23,24]. Based on the above dilemma, the design idea of effectively improving the optical absorption

range of  $\text{Co}_3\text{O}_4$  and increasing the separation rate of photogenerated carriers may enable it to meet the demand gap in the field of environmental governance.

For a long time, researchers have also actively carried out a lot of research based on light absorption and carrier separation [25,26]. The implementation of many technical strategies, such as the design of morphologies, the construction of heterostructures, and the modification of precious metals, greatly optimized and improved the photocatalytic performance of  $\text{Co}_3\text{O}_4$ . Among them, the construction of semiconductor heterostructures is the most effective way to promote efficient carrier separation and migration and has shown impressive performance in many reports [24,27]. In these heterostructures, the p-type semiconductor  $\text{Co}_3\text{O}_4$  conduction band (CB) and valence band (VB) bend towards vacuum level while the n-type semiconductor bend against vacuum level due to the formation of the built-in electric field in the catalyst and the balance of Fermi energy levels [28,29]. Moreover, the bending is only large at the region far from the depletion region. Driven by the force of the electric field, the charge is further separated efficiently, thus improving the photocatalytic efficiency. At present, the various reported n-type semiconductors that have been used to construct the p-type semiconductor  $\text{Co}_3\text{O}_4$  include g- $\text{C}_3\text{N}_4$  [11,30],  $\text{In}_2\text{O}_3$  [31],  $\text{Bi}_2\text{O}_3$  [32], and  $\text{MnO}_2$  [33]. Graphitic carbon nitride, a stable polymer semiconductor with a special 2D framework structure of heptazine rings connected via tertiary amines, could form a self-built internal electrostatic field, and the electric field and van der Waals interactions cause photogenerated separation and transport of carriers [29,34]. Moreover, due to its wide band gap, g- $\text{C}_3\text{N}_4$  exhibits efficient sunlight collection properties. And thanks to its sparse and porous structure, it is also able to easily adsorb and re-degrade pollutants [35]. Therefore, the modification of g- $\text{C}_3\text{N}_4$ -based materials gives us a more practical pathway to enhance the activity of metal oxides. Based on this, we are eager to learn whether the coupling between g- $\text{C}_3\text{N}_4$  and  $\text{Co}_3\text{O}_4$  could efficiently solve problems in the field of environmental treatment.

In our research,  $\text{Co}_3\text{O}_4$  nanosheets and g- $\text{C}_3\text{N}_4$  were prepared by a rapid hydrothermal method and a calcination method, respectively, and then  $\text{Co}_3\text{O}_4$ /g- $\text{C}_3\text{N}_4$  nanomaterials were prepared by composing the two. The microstructure and physical and chemical properties of  $\text{Co}_3\text{O}_4$ /g- $\text{C}_3\text{N}_4$  were characterized by several methods, such as HRTEM, XPS, BET, and ESR, and the performance of different mass ratios of  $\text{Co}_3\text{O}_4$ /g- $\text{C}_3\text{N}_4$  on the catalyst photodegradation activity of RhB was investigated under simulated sunlight. The results showed that the photocatalytic activity of  $\text{Co}_3\text{O}_4$ /g- $\text{C}_3\text{N}_4$  was significantly enhanced compared with that of the pure sample, which may be due to the role of the heterojunction established between  $\text{Co}_3\text{O}_4$  and g- $\text{C}_3\text{N}_4$ , which could promote the separation of photogenerated charges and interfacial effects. Finally, a possible charge transfer pathway is proposed based on the experimental results. Our work offers new insights into the application of crystalline semiconductors for the removal of aqueous organic pollutants.

## 2. Materials and Methods

### 2.1. Materials

$\text{CO}(\text{NH}_2)_2$ ,  $\text{Co}(\text{NO}_3)_2 \cdot 6\text{H}_2\text{O}$ ,  $\text{C}_2\text{H}_6\text{O}$ ,  $\text{NaOH}$ ,  $\text{C}_2\text{H}_3\text{N}$ ,  $\text{C}_6\text{H}_{15}\text{NO}_3$ , and  $\text{C}_{28}\text{H}_{31}\text{ClN}_2\text{O}_3$  were procured from Sinopharm Chemical Reagent Co., Ltd. (Shanghai, China).  $(\text{C}_6\text{H}_9\text{NO})_n$  (M.W.  $\approx 55,000$ ) was acquired from Aladdin Reagent Co., Ltd. (Shanghai, China). Deionized water was used throughout the experiment. All chemicals were analytically pure and required no further processing.

### 2.2. Synthesis of g- $\text{C}_3\text{N}_4$

Urea (20 g sample) was added to a 50 mL crucible container and transferred to a muffle furnace and calcined under an air atmosphere. The conditions were set to increase from ambient temperature to 823 K at a rate of 5 K/min for 4 h. After the sample cooled down, the sample was made into powder with a mortar and raised from the initial temperature to 773 K at a rate of 5 K/min for 2 h. The light-yellow powder obtained was g- $\text{C}_3\text{N}_4$ , named CN.

### 2.3. Synthesis of $\beta\text{-Co(OH)}_2$

$\text{Co(NO}_3)_2 \cdot 6\text{H}_2\text{O}$  and  $(\text{C}_6\text{H}_9\text{NO})_n$  (PVP, M.W.  $\approx 55,000$ ) were thoroughly mixed in absolute ethanol and deionized water for 1 h. The mixture was then transferred to a 25 mL Teflon-lined autoclave. It was reacted for 12 h at 473 K before being cooled to room temperature. The pink product was washed several times with deionized water and anhydrous ethanol until the pH of the filtrate reached neutral, and then vacuum dried for 14 h.

### 2.4. Synthesis of $\text{Co}_3\text{O}_4$

The  $\beta\text{-Co(OH)}_2$  precursor was heated in a tube furnace at a rate of 5 K/min and kept at 673 K for 2 h. The obtained product was the labeled  $\text{Co}_3\text{O}_4$  nanosheet.

### 2.5. Synthesis of $\text{Co}_3\text{O}_4/\text{g-C}_3\text{N}_4$

The deionized water was added into the above-prepared  $\text{Co}_3\text{O}_4$  and g-C<sub>3</sub>N<sub>4</sub> and mixed with stirring, and a series of  $\text{Co}_3\text{O}_4/\text{g-C}_3\text{N}_4$  mixture samples with different ratios were synthesized by adjusting the mass ratio between  $\text{Co}_3\text{O}_4$  and g-C<sub>3</sub>N<sub>4</sub>. After being rapidly frozen with liquid nitrogen, the samples were dried in a freeze-drying oven for 72 h.

## 3. Results and Discussion

### 3.1. Microscopic Morphology and Chemical Structure Characterization

The synthesis route of the  $\text{Co}_3\text{O}_4/\text{g-C}_3\text{N}_4$  sample is displayed in Figure 1. Here, urea was thermally oxidized to obtain g-C<sub>3</sub>N<sub>4</sub> sample. At the same time,  $\beta\text{-Co(OH)}_2$  was prepared by solvothermal reaction as a precursor of  $\text{Co}_3\text{O}_4$ . Eventually, the  $\text{Co}_3\text{O}_4/\text{g-C}_3\text{N}_4$  heterojunction was produced by liquid nitrogen-assisted thermal oxidation.

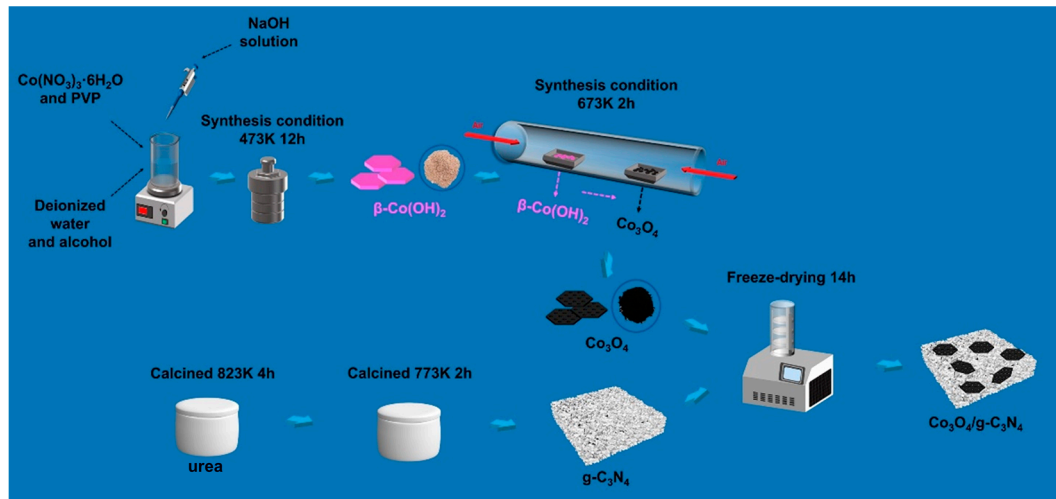


**Figure 1.** Schematic graph of the synthesis route of  $\text{Co}_3\text{O}_4/\text{g-C}_3\text{N}_4$ .

X-ray diffraction (XRD) was used to analyze crystallographic structures of samples in Figure 2a. It can be seen that g-C<sub>3</sub>N<sub>4</sub> has broad peaks at  $13.2^\circ$  and  $27.6^\circ$ , corresponding to the (100) and (002) crystal planes of g-C<sub>3</sub>N<sub>4</sub> (JCPDS No. 87-1526), and the  $\text{Co}_3\text{O}_4/\text{g-C}_3\text{N}_4$  catalyst exhibits only very weak  $\text{Co}_3\text{O}_4$  diffraction peaks due to the low loading percentage of the  $\text{Co}_3\text{O}_4$  catalyst (JCPDS No. 09-0418). Five characteristic peaks were identified at  $2\theta = 31.3^\circ$  ( $d = 2.86 \text{ \AA}$ ),  $36.85^\circ$  ( $d = 2.44 \text{ \AA}$ ),  $55.64^\circ$  ( $d = 1.65 \text{ \AA}$ ),  $59.35^\circ$  ( $d = 1.56 \text{ \AA}$ ), and  $65.22^\circ$  ( $d = 1.43 \text{ \AA}$ ) corresponding to (220), (311), (422), (511), and (440) as cubic  $\text{Co}_3\text{O}_4$  crystal faces [11]. The transmission electron microscopy (TEM) image of 5%  $\text{Co}_3\text{O}_4/\text{g-C}_3\text{N}_4$  was shown in Figure 2b, where  $\text{Co}_3\text{O}_4$  nanosheets of about 150–200 nm in size can be observed on the surface of g-C<sub>3</sub>N<sub>4</sub>. HRTEM and corresponding FFT studies were performed for 5%  $\text{Co}_3\text{O}_4/\text{g-C}_3\text{N}_4$  (Figure 2c,d), and the lattice stripes with spacing of 0.285 and 0.466 nm

correspond to the (220) and (111) crystal planes of  $\text{Co}_3\text{O}_4$  (JCPDS No. 09-0418) [20]. In summary, a clear interface existed between  $\text{Co}_3\text{O}_4$  and g- $\text{C}_3\text{N}_4$ , and the interfacial contact facilitates the rapid transfer of photogenerated charges.

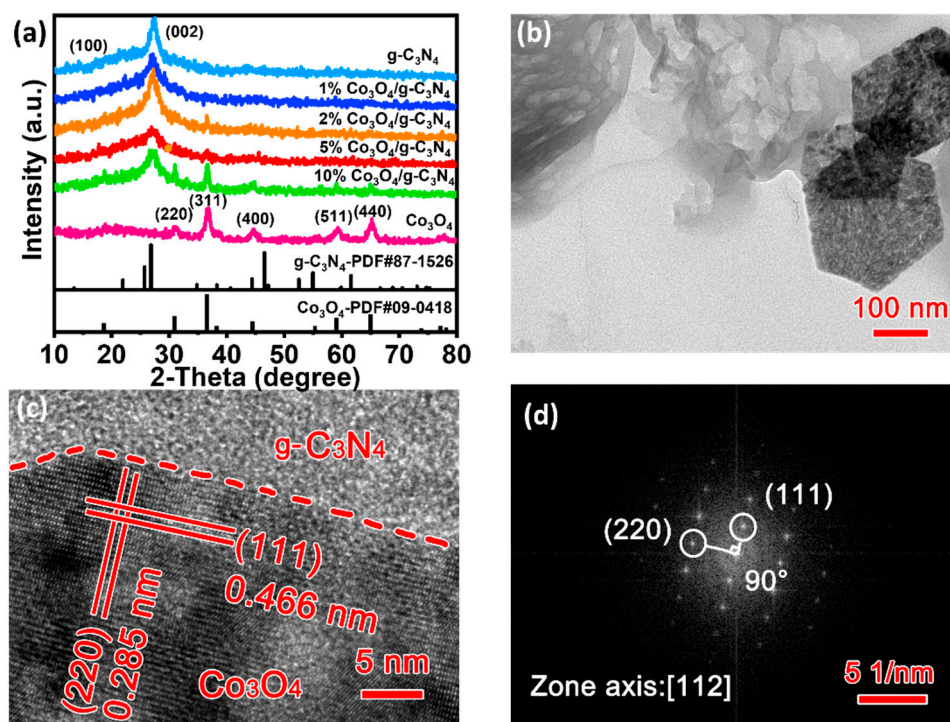


**Figure 2.** (a) XRD patterns; (b) TEM; (c,d) HRTEM and corresponding FFT images of 5%  $\text{Co}_3\text{O}_4/\text{g-C}_3\text{N}_4$ .

The analysis of X-ray photoelectron spectroscopy (XPS) provides insight into the surface composition and chemical changes in each sample. From the full survey spectra of samples in Figure 3a, it was found that Co, C, N, and O elements were detected in 5%  $\text{Co}_3\text{O}_4/\text{g-C}_3\text{N}_4$ , and the molar ratio of C:N:O:Co in 5%  $\text{Co}_3\text{O}_4/\text{g-C}_3\text{N}_4$  was about 48:49.6:2:0.3, which further confirmed the complexation of  $\text{Co}_3\text{O}_4$  with g- $\text{C}_3\text{N}_4$ . The high-resolution XPS spectra of the C 1s spectra at energies of 288.11 eV, 286.54 eV, and 284.66 eV belong to the C-O bond and the N-C=N bond in Figures 3b and S1. The peaks of the N 1s spectra (Figure 3c) are located at 404.71 eV, 400.47 eV, 399.06 eV, and 398.43 eV, respectively, which can be attributed to  $\text{sp}^2$ -hybridized nitrogen C-N=C, tertiary nitrogen N-(C)<sub>3</sub>, and primary nitrogen H-N-(C)<sub>2</sub> [10,12]. The peaks of the O 1s spectra can be shown in Figure 3d, except peaks at 530.38 and 529.17 eV and at 532.35 and 531.42 eV can be found, which originate from the O-C=O and C-O groups produced at the interface of  $\text{Co}_3\text{O}_4$  and g- $\text{C}_3\text{N}_4$  [33,36]. The Co 1s energy spectra of  $\text{Co}_3\text{O}_4$  and the Co 2p energy spectra of 5%  $\text{Co}_3\text{O}_4/\text{g-C}_3\text{N}_4$  samples (Figure 3e) showed four characteristic peaks at 795.13 eV, 794.03 eV, 780.03 eV, and 778.68 eV, which can be ascribed to the Co-O and Co=O bonds [27,37]. The effect of photocatalytic degradation is influenced by the specific surface area of the material, and the surface area of different samples was investigated by the  $\text{N}_2$  adsorption–desorption technique (BET). The g- $\text{C}_3\text{N}_4$  exhibits a typical type IV isotherm with H3-type hysteresis loops, and its mesoporous structure may be due to the stacking of the g- $\text{C}_3\text{N}_4$  (Figure 3f). The surface area of g- $\text{C}_3\text{N}_4$  is about 128.5  $\text{m}^2/\text{g}$  as calculated by the model that comes with the instrument. The higher specific surface area is attributed to the large-scale nanosheet morphology of g- $\text{C}_3\text{N}_4$ . The specific surface area of the 5%  $\text{Co}_3\text{O}_4/\text{g-C}_3\text{N}_4$  composite was slightly decreased after combining with  $\text{Co}_3\text{O}_4$ , probably since the decrease in specific surface area caused by the interfacial contact between  $\text{Co}_3\text{O}_4$  and g- $\text{C}_3\text{N}_4$ . The interfacial effect of 5%  $\text{Co}_3\text{O}_4/\text{g-C}_3\text{N}_4$  promotes the adsorption of pollutants by the catalyst, and the abundant active sites are conducive to efficient photocatalytic reactions.



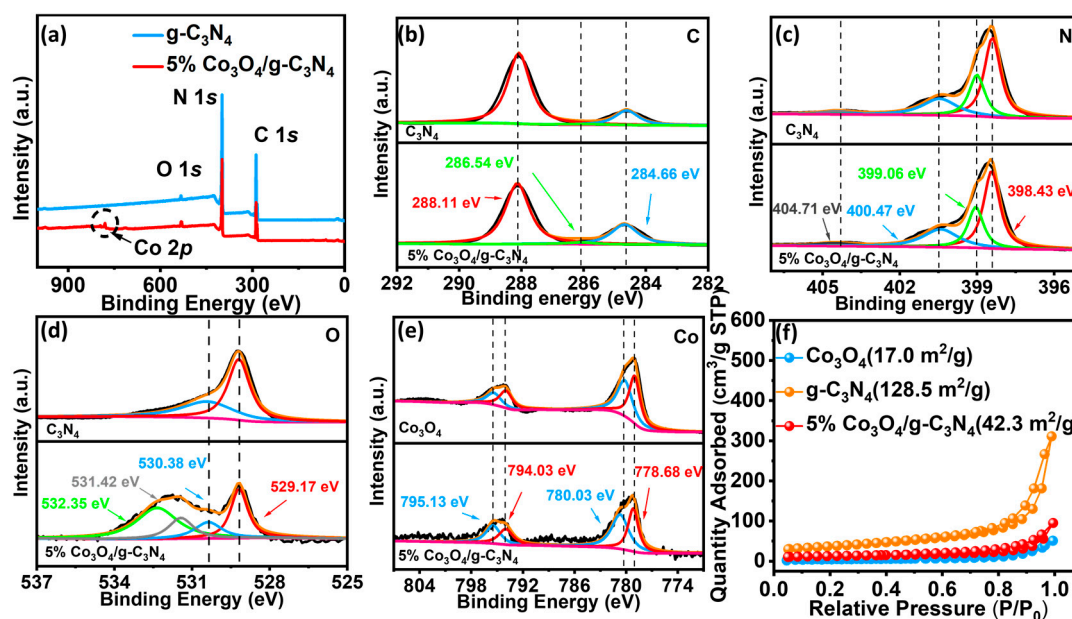


**Figure 3.** XPS spectra of (a) samples; (b) C 1s; (c) N 1s; (d) O 1s; (e) Co 2p; (f)  $N_2$  adsorption-desorption technique.

### 3.2. Performance Analysis and Kinetics Study of RhB Degradation by Photocatalytic Application

The photodegradation RhB activity of different proportions of samples is usually tested under simulated sunlight conditions. As shown in Figure 4a, the degradation effect of RhB after 40 min under different sample light conditions, demonstrates that the heterogeneous combination of g-C<sub>3</sub>N<sub>4</sub> and Co<sub>3</sub>O<sub>4</sub> effectively promoted the photocatalytic reaction. Among them, the degradation of RhB by 5% Co<sub>3</sub>O<sub>4</sub>/g-C<sub>3</sub>N<sub>4</sub> can reach 97.6%. At low concentrations, more Co<sub>3</sub>O<sub>4</sub> facilitates the rapid carrier transfer and promotes the photocatalytic degradation reaction. However, when the concentration is high, Co<sub>3</sub>O<sub>4</sub> covers the surface of g-C<sub>3</sub>N<sub>4</sub>, which hinders its light absorption and obscures the active site, thus causing a decrease in the reaction activity. Figure 4b shows the variation of different proportions in the samples, photocatalytic degradation of RhB over time, which more clearly confirms that the catalytic ability of 5% Co<sub>3</sub>O<sub>4</sub>/g-C<sub>3</sub>N<sub>4</sub> is stronger than additional two monomeric catalysts. Based on the above characterization, a reaction kinetic model was established (Figure 4c), and the perfect linear relationship between  $\ln(C_0/C)$  and irradiation time indicates that the photocatalytic reaction is the quasi-primary reaction; g-C<sub>3</sub>N<sub>4</sub>, Co<sub>3</sub>O<sub>4</sub> and 5% Co<sub>3</sub>O<sub>4</sub>/g-C<sub>3</sub>N<sub>4</sub> have rate constants  $k$  values of 0.024 min<sup>−1</sup>, 0.0126 min<sup>−1</sup>, and 0.0703 min<sup>−1</sup>, respectively. The degradation efficiency of 5% Co<sub>3</sub>O<sub>4</sub>/g-C<sub>3</sub>N<sub>4</sub> is approximately 3 times that of g-C<sub>3</sub>N<sub>4</sub> and 5.58 times that of Co<sub>3</sub>O<sub>4</sub>. The Co<sub>3</sub>O<sub>4</sub>/g-C<sub>3</sub>N<sub>4</sub> exhibited better photocatalytic activity than most of the reported photoreduction systems under similar conditions (Table S1). In addition, the repeatability of the 5% Co<sub>3</sub>O<sub>4</sub>/g-C<sub>3</sub>N<sub>4</sub> material was tested in Figure 4d. It can be shown that the performance of 5% Co<sub>3</sub>O<sub>4</sub>/g-C<sub>3</sub>N<sub>4</sub> did not show significant degradation after three cycles, which proved the excellent stability of the composite through interfacial compounding.

Testing the UV-vis diffuse reflectance spectroscopy (DRS) of catalysts can provide insight into their light absorption capabilities and help in studying their optical properties. It can be seen from Figure 5a, the absorption edge of g-C<sub>3</sub>N<sub>4</sub> is about 450 nm, and there is almost no response in visible region beyond 450 nm. However, the absorption of 5% Co<sub>3</sub>O<sub>4</sub>/g-C<sub>3</sub>N<sub>4</sub> is significantly stronger in visible light due to the interfacial effect formed between Co<sub>3</sub>O<sub>4</sub> and g-C<sub>3</sub>N<sub>4</sub>, which helps to improve the photocatalytic activity of the catalyst [38–40]. The photoluminescence (PL) spectra show that the fluorescence intensities of g-C<sub>3</sub>N<sub>4</sub> and Co<sub>3</sub>O<sub>4</sub> were significantly higher than 5% Co<sub>3</sub>O<sub>4</sub>/g-C<sub>3</sub>N<sub>4</sub>, which indicates a higher complexation rate of photogenerated carriers on Co<sub>3</sub>O<sub>4</sub> and g-C<sub>3</sub>N<sub>4</sub> [41,42] (Figure 5b). To further demonstrate that 5% Co<sub>3</sub>O<sub>4</sub>/g-C<sub>3</sub>N<sub>4</sub> has better photogenerated

charge separation efficiency, the time-dependent photocurrent of samples was analyzed. The 5%  $\text{Co}_3\text{O}_4/\text{g-C}_3\text{N}_4$  catalyst exhibited a higher photocurrent response intensity compared with single  $\text{g-C}_3\text{N}_4$ , which indicates that the composite catalyst promotes the separation and transfer of photogenerated electron–hole pairs in Figure 5c. Furthermore, the 5%  $\text{Co}_3\text{O}_4/\text{g-C}_3\text{N}_4$  catalyst also has a smaller arc radius in the Nyquist plot of electrochemical impedance spectroscopy (EIS), which further suggests that the 5%  $\text{Co}_3\text{O}_4/\text{g-C}_3\text{N}_4$  catalyst has better photogenerated carrier separation efficiency (Figures 5d and S2) [43,44]. Therefore, the stronger photocurrent response and the smaller charge transfer impedance suggest that the photogenerated electron–hole pairs can be effectively separated in 5%  $\text{Co}_3\text{O}_4/\text{g-C}_3\text{N}_4$ .

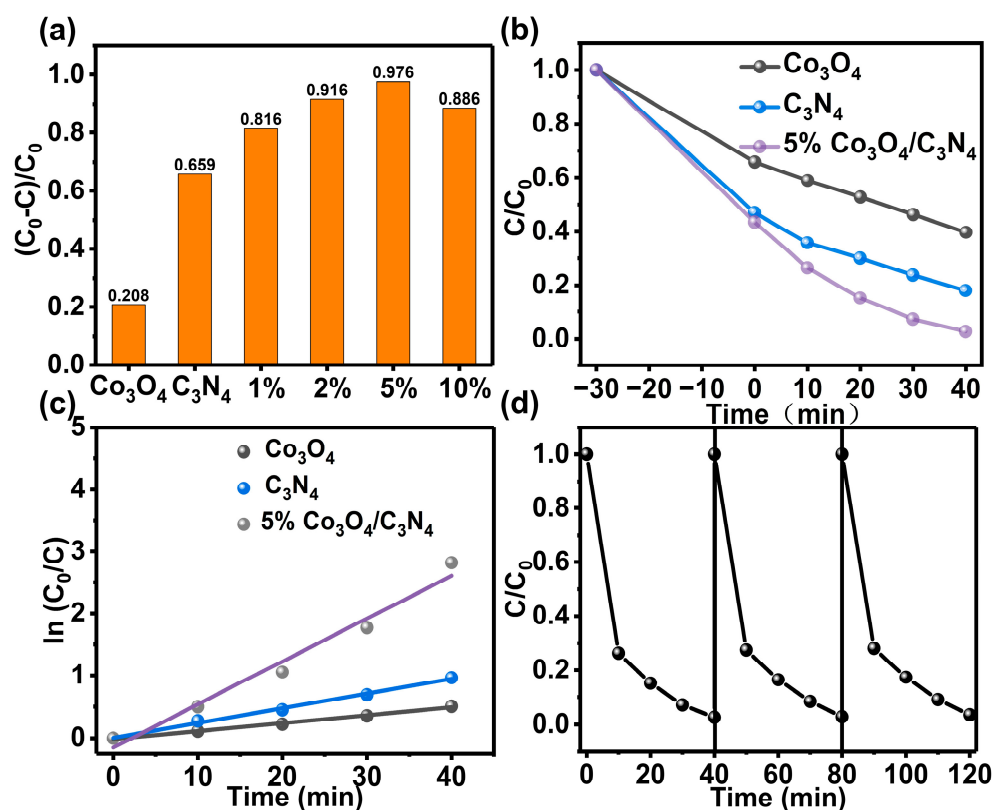


**Figure 4.** (a) Photodegradation rate of RhB by different samples under simulated sunlight for 40 min; (b)  $\text{g-C}_3\text{N}_4$ ,  $\text{Co}_3\text{O}_4$  and 5%  $\text{Co}_3\text{O}_4/\text{g-C}_3\text{N}_4$  photocatalytic degradation of RhB with time; (c) photocatalytic reaction kinetics; (d) stability test of 5%  $\text{Co}_3\text{O}_4/\text{g-C}_3\text{N}_4$ .

Based on the XPS valence band (XPS-VB) spectral analysis, the VB maxima of  $\text{Co}_3\text{O}_4$  and  $\text{g-C}_3\text{N}_4$  can be determined to be  $-0.15$  and  $2.17$  eV, respectively (Figure 6a); therefore, the conduction band (CB) minima of  $\text{Co}_3\text{O}_4$  and  $\text{g-C}_3\text{N}_4$  can be easily calculated as  $-2.92$  and  $-3.08$  eV. By analyzing the DRS spectra, the bandgaps ( $E_g$ ) of  $\text{Co}_3\text{O}_4$  and  $\text{g-C}_3\text{N}_4$  were obtained to be  $1.3$  and  $2.98$  eV, respectively (Figure 6b). Based on the above analysis, a type-II heterojunction [2] photocatalytic mechanism is proposed in Figure 6c. The 5%  $\text{Co}_3\text{O}_4/\text{g-C}_3\text{N}_4$  photocatalyst was excited beneath light irradiation and generates electron and hole pairs, and transferred the electrons from the CB of  $\text{Co}_3\text{O}_4$  to  $\text{g-C}_3\text{N}_4$ . Thanks to the intrinsic force field shaped by interface contact between  $\text{Co}_3\text{O}_4$  and  $\text{g-C}_3\text{N}_4$ , whereas the holes on the VB of  $\text{g-C}_3\text{N}_4$  are often transferred to  $\text{Co}_3\text{O}_4$ . The  $\text{Co}_3\text{O}_4$  can produce more photogenerated electrons on the CB of  $\text{g-C}_3\text{N}_4$  that can promote the conversion of superoxide radicals ( $\bullet\text{O}_2^-$ ) and accelerate the conversion of RhB to the subsequent mineralization products.

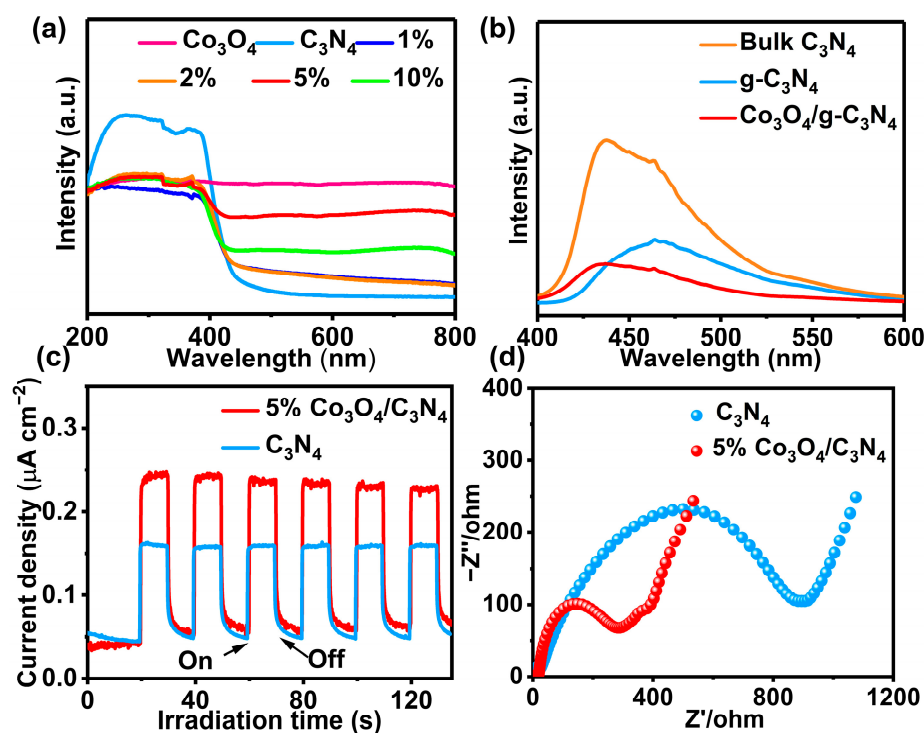


Figure 5. (a) DRS spectra, (b) PL spectra; (c) photocurrent responses, and (d) EIS measurement of samples.

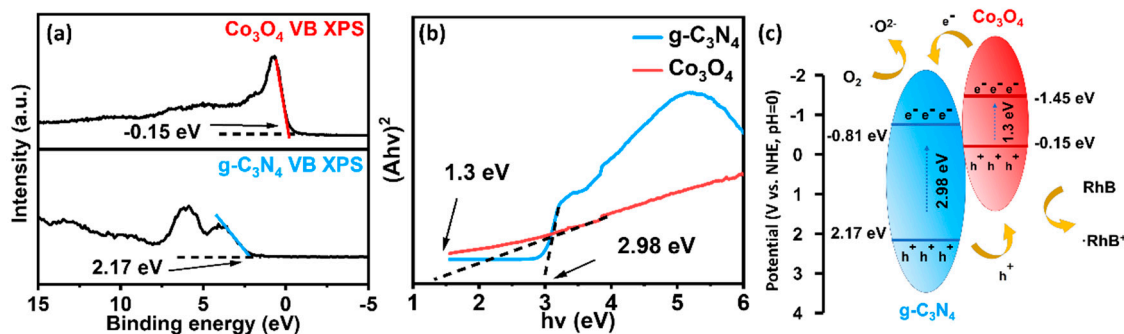
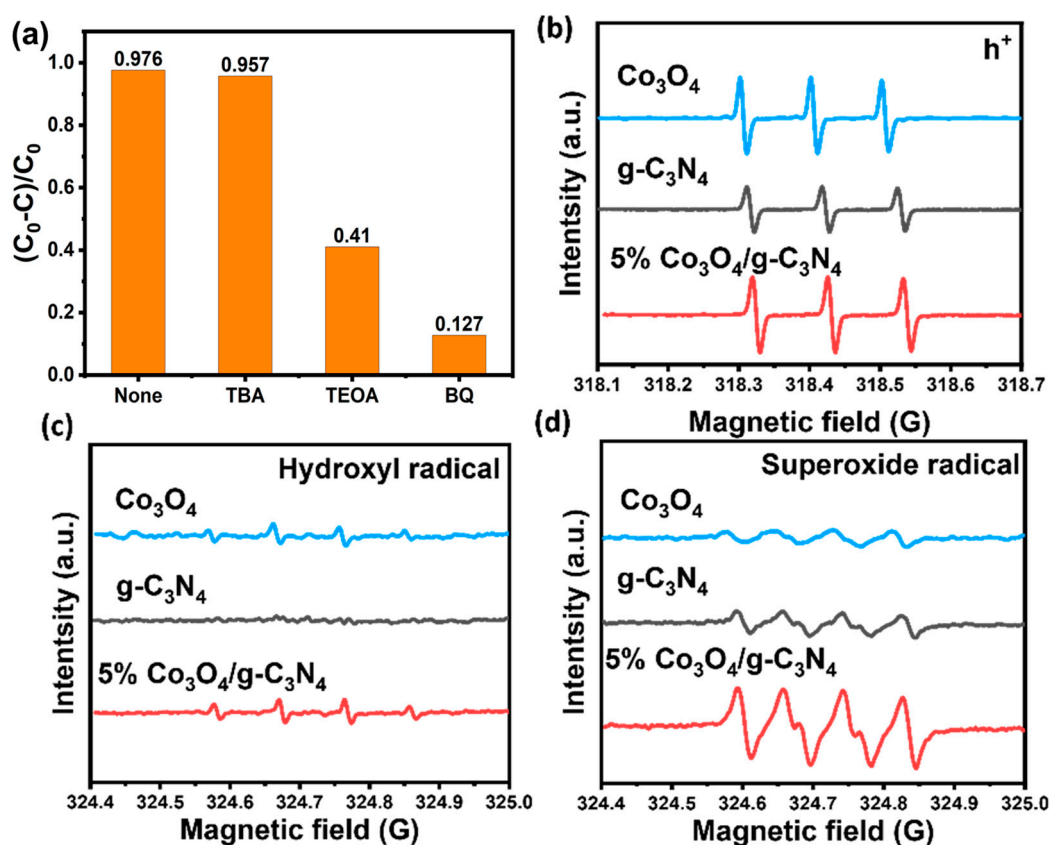


Figure 6. (a) XPS-VB spectra of  $\text{Co}_3\text{O}_4$  and  $\text{g-C}_3\text{N}_4$ ; (b) Tauc plots of  $\text{Co}_3\text{O}_4$  and  $\text{g-C}_3\text{N}_4$ ; (c)  $\text{Co}_3\text{O}_4$  and  $\text{g-C}_3\text{N}_4$  electronic band structures and schematic diagram of electrons transfer paths.

To explore the active species in the 5%  $\text{Co}_3\text{O}_4/\text{g-C}_3\text{N}_4$  photocatalytic degradation of RhB, a series of free radical capturing experiments was performed (Figure 7a). Tertiary butanol (TBA), triethanolamine (TEOA), and benzoquinone (BQ) were used as the capture agents of  $\bullet\text{OH}$ ,  $\text{h}^+$  and  $\bullet\text{O}_2^-$ . After 40 min of light irradiation, it was found that the degradation efficiency of RhB by 5%  $\text{Co}_3\text{O}_4/\text{g-C}_3\text{N}_4$  was significantly inhibited by the addition of TEOA and BQ, while the degradation effect did not change significantly after the addition of TBA. The radical capturing experiments indicated that the active species within the degradation of RhB by 5%  $\text{Co}_3\text{O}_4/\text{g-C}_3\text{N}_4$  were in the main  $\bullet\text{O}_2^-$  and  $\text{h}^+$ , however not  $\bullet\text{OH}$ . In order to further verify the results, an electron spin resonance (ESR) analysis was carried out. After 10 min of irradiation with a Xe lamp (300 W), the 5%  $\text{Co}_3\text{O}_4/\text{g-C}_3\text{N}_4$  surface produced strong  $\bullet\text{O}_2^-$  and  $\text{h}^+$  signals (Figure 7b,c), while almost no signal of  $\bullet\text{OH}$  appeared (Figure 7d), proving that  $\bullet\text{O}_2^-$  and  $\text{h}^+$  are the main reactive groups in the reaction system, which is in line with the results of the radical capturing experiments. In addition, it was often found that the signals of  $\bullet\text{O}_2^-$  and  $\text{h}^+$  on the surface of 5%  $\text{Co}_3\text{O}_4/\text{g-C}_3\text{N}_4$  significantly exceeded those of  $\text{g-C}_3\text{N}_4$ , indicating that the created heterojunction will higher separate the photogenerated carriers, confirming the results of the previous analysis.



**Figure 7.** (a) Photodegradation rate of RhB by 5%  $\text{Co}_3\text{O}_4/\text{g-C}_3\text{N}_4$  under different scavengers within 40 min; ESR spectra of  $\text{g-C}_3\text{N}_4$ ,  $\text{Co}_3\text{O}_4$  and 5%  $\text{Co}_3\text{O}_4/\text{g-C}_3\text{N}_4$  (b) holes; (c) hydroxyl radicals; (d) superoxide radicals.

#### 4. Conclusions

In summary, a novel type-II heterojunction photocatalyst ( $\text{Co}_3\text{O}_4/\text{g-C}_3\text{N}_4$ ) was prepared by simple hydrothermal and calcination methods and used to efficiently degrade RhB in water. The experimental results showed that the  $\text{Co}_3\text{O}_4/\text{g-C}_3\text{N}_4$  photocatalyst had robust photocatalytic degradation activity toward RhB under light irradiation. The DRS, PL, time-dependent photocurrent, and EIS analyses revealed that the type-II heterojunction structure effectively reduced the composite rate of photogenerated electrons and holes, and therefore the holes in VB of  $\text{Co}_3\text{O}_4$  and therefore the electrons in CB of  $\text{g-C}_3\text{N}_4$  were utilized to reinforce the oxidation–reduction ability of the photocatalyst, which resulted in the speedy degradation of pollutants. Among them, the best degradation potency was achieved by a 5%  $\text{Co}_3\text{O}_4/\text{g-C}_3\text{N}_4$  photocatalyst, and the RhB degradation potency was increased by 48% compared with the  $\text{g-C}_3\text{N}_4$  photocatalyst. This study provides some reference data for the development of different heterojunction photocatalysts for the degradation of organic pollutants.

**Supplementary Materials:** The following supporting information can be downloaded at: <https://www.mdpi.com/article/10.3390/ma16103879/s1>. Characterization of the photocatalysts. Photoelectrochemical test. Photocatalytic degradation activity test. Figure S1. The high-resolution O 1s spectra of  $\text{Co}_3\text{O}_4$ . Figure S2. EIS spectra under light conditions. Table S1. Common photocatalyst and the effect of degrading organic pollutants in water. Refs [45–54] were cited in the Supplementary Materials.

**Author Contributions:** Y.D.: Methodology, Conceptualization, Investigation, Data curation, Writing—original draft. Z.F.: Investigation, Data curation, Writing—review and editing. K.Z.: Writing—review and editing. J.T.: Writing—review and editing, Investigation. G.W.: Writing—review and editing. Q.L.: Writing—review and editing. Z.W.: Writing—review and editing. Y.H.: Investigation. J.L.:



Project administration, Methodology. H.X.: Resources, Funding acquisition, Methodology, Writing—review and editing. X.Z.: Supervision, Project administration, Writing—review and editing, Funding acquisition. All authors have read and agreed to the published version of the manuscript.

**Funding:** This study was funded by the Natural Science Foundation of Jiangsu Province (BK20220598), Key Laboratory of Electrochemical Energy Storage and Energy Conversion of Hainan Province (KFKT2022001).

**Institutional Review Board Statement:** Not applicable.

**Informed Consent Statement:** Not applicable.

**Data Availability Statement:** Raw data are available upon request.

**Conflicts of Interest:** The authors declare that they have no known competing financial interest or personal relationships that could have appeared to influence the work reported in this paper.

## References

- Chen, C.; Ma, W.; Zhao, J. Semiconductor-mediated photodegradation of pollutants under visible-light irradiation. *Chem. Soc. Rev.* **2010**, *39*, 4206–4219. [\[CrossRef\]](#)
- Li, X.; Yu, J.; Jaroniec, M. Hierarchical photocatalysts. *Chem. Soc. Rev.* **2016**, *45*, 2603–2636. [\[CrossRef\]](#)
- Jing, L.; Xu, Y.; Liu, J.; Zhou, M.; Xu, H.; Xie, M.; Li, H.; Xie, J. Direct Z-scheme red carbon nitride/rod-like lanthanum vanadate composites with enhanced photodegradation of antibiotic contaminants. *Appl. Catal. B Environ.* **2020**, *277*, 119245. [\[CrossRef\]](#)
- Jing, L.; He, M.; Xie, M.; Song, Y.; Wei, W.; Xu, Y.; Xu, H.; Li, H. Realizing the synergistic effect of electronic modulation over graphitic carbon nitride for highly efficient photodegradation of bisphenol A and 2-mercaptobenzothiazole: Mechanism, degradation pathway and density functional theory calculation. *J. Colloid Interface Sci.* **2021**, *583*, 113–127. [\[CrossRef\]](#) [\[PubMed\]](#)
- Jing, L.; Xu, Y.; Zhou, M.; Deng, J.; Wei, W.; Xie, M.; Song, Y.; Xu, H.; Li, H. Novel broad-spectrum-driven oxygen-linked band and porous defect co-modified orange carbon nitride for photodegradation of Bisphenol A and 2-Mercaptobenzothiazole. *J. Hazard. Mater.* **2020**, *396*, 122659. [\[CrossRef\]](#)
- Kubacka, A.; Fernández-García, M.; Colón, G. Advanced nanoarchitectures for solar photocatalytic applications. *Chem. Rev.* **2012**, *112*, 1555–1614. [\[CrossRef\]](#)
- Schneider, J.; Matsuoka, M.; Takeuchi, M.; Zhang, J.; Horiuchi, Y.; Anpo, M.; Bahnemann, D.W. Understanding TiO<sub>2</sub> photocatalysis: Mechanisms and materials. *Chem. Rev.* **2014**, *114*, 9919–9986. [\[CrossRef\]](#) [\[PubMed\]](#)
- Wang, L.; Li, D.-B.; Li, K.; Chen, C.; Deng, H.-X.; Gao, L.; Zhao, Y.; Jiang, F.; Li, L.; Huang, F.; et al. Stable 6%-efficient Sb<sub>2</sub>Se<sub>3</sub> solar cells with a ZnO buffer layer. *Nat. Energy* **2017**, *2*, 17046. [\[CrossRef\]](#)
- Fu, J.; Jiang, K.; Qiu, X.; Yu, J.; Liu, M. Product Cocatalysts of photocatalytic CO<sub>2</sub> reduction reactions. *Mater. Today* **2020**, *32*, 222–243. [\[CrossRef\]](#)
- Zhu, X.; Yang, J.; She, X.; Song, Y.; Qian, J.; Wang, Y.; Xu, H.; Li, H.; Yan, Q. Rapid synthesis of ultrathin 2D materials through liquid-nitrogen and microwave treatments. *J. Mater. Chem. A* **2019**, *7*, 5209–5213. [\[CrossRef\]](#)
- Zhu, X.; Ji, H.; Yi, J.; Yang, J.; She, X.; Ding, P.; Li, L.; Deng, J.; Qian, J.; Xu, H.; et al. A Specifically Exposed Cobalt Oxide/Carbon Nitride 2D Heterostructure for Carbon Dioxide Photoreduction. *Ind. Eng. Chem. Res.* **2018**, *57*, 17394–17400. [\[CrossRef\]](#)
- Mo, Z.; Zhu, X.; Jiang, Z.; Song, Y.; Liu, D.; Li, H.; Yang, X.; She, Y.; Lei, Y.; Yuan, S.; et al. Porous nitrogen-rich g-C<sub>3</sub>N<sub>4</sub> nanotubes for efficient photocatalytic CO<sub>2</sub> reduction. *Appl. Catal. B Environ.* **2019**, *256*, 117854. [\[CrossRef\]](#)
- Zhou, X.; Zhang, X.; Ding, P.; Zhong, K.; Yang, J.; Yi, J.; Hu, Q.; Zhou, G.; Wang, X.; Xu, H.; et al. Simultaneous manipulation of scalable absorbance and the electronic bridge for efficient CO<sub>2</sub> photoreduction. *J. Mater. Chem. A* **2022**, *10*, 25661–25670. [\[CrossRef\]](#)
- Yang, J.; Jing, L.; Zhu, X.; Zhang, W.; Deng, J.; She, Y.; Nie, K.; Wei, Y.; Li, H.; Xu, H. Modulating electronic structure of lattice O-modified orange polymeric carbon nitrogen to promote photocatalytic CO<sub>2</sub> conversion. *Appl. Catal. B Environ.* **2023**, *320*, 122005. [\[CrossRef\]](#)
- Zhu, C.; Xian, Q.; He, Q.; Chen, C.; Zou, W.; Sun, C.; Wang, S.; Duan, X. Edge-Rich Bicrystalline 1T/2H-MoS<sub>2</sub> Cocatalyst-Decorated {110} Terminated CeO<sub>2</sub> Nanorods for Photocatalytic Hydrogen Evolution. *ACS Appl. Mater. Interfaces* **2021**, *13*, 35818–35827. [\[CrossRef\]](#) [\[PubMed\]](#)
- Xu, H.; Yi, J.; She, X.; Liu, Q.; Song, L.; Chen, S.; Yang, Y.; Song, Y.; Vajtai, R.; Lou, J.; et al. 2D heterostructure comprised of metallic 1T-MoS<sub>2</sub>/Monolayer O-g-C<sub>3</sub>N<sub>4</sub> towards efficient photocatalytic hydrogen evolution. *Appl. Catal. B Environ.* **2018**, *220*, 379–385. [\[CrossRef\]](#)
- Zhu, Z.; Li, X.; Qu, Y.; Zhou, F.; Wang, Z.; Wang, W.; Zhao, C.; Wang, H.; Li, L.; Yao, Y.; et al. A hierarchical heterostructure of CdS QDs confined on 3D ZnIn<sub>2</sub>S<sub>4</sub> with boosted charge transfer for photocatalytic CO<sub>2</sub> reduction. *Nano Res.* **2021**, *14*, 81–90. [\[CrossRef\]](#)
- Naya, S.-I.; Kume, T.; Akashi, R.; Fujishima, M.; Tada, H. Red-Light-Driven Water Splitting by Au(Core)-CdS(Shell) Half-Cut Nanoegg with Heteroepitaxial Junction. *J. Am. Chem. Soc.* **2018**, *140*, 1251–1254. [\[CrossRef\]](#)
- Li, J.-X.; Ye, C.; Li, X.-B.; Li, Z.-J.; Gao, X.-W.; Chen, B.; Tung, C.-H.; Wu, L.-Z. A Redox Shuttle Accelerates O<sub>2</sub> Evolution of Photocatalysts Formed In Situ under Visible Light. *Adv. Mater.* **2017**, *29*, 1606009. [\[CrossRef\]](#)

20. Hu, L.; Peng, Q.; Li, Y. Selective Synthesis of  $\text{Co}_3\text{O}_4$  Nanocrystal with Different Shape and Crystal Plane Effect on Catalytic Property for Methane Combustion. *J. Am. Chem. Soc.* **2008**, *130*, 16136–16137. [\[CrossRef\]](#)
21. Liu, G.; Wang, L.; Chen, X.; Zhu, X.; Wang, B.; Xu, X.; Chen, Z.; Zhu, W.; Li, H.; Xia, J. Crafting of plasmonic Au nanoparticles coupled ultrathin BiOBr nanosheets heterostructure: Steering charge transfer for efficient  $\text{CO}_2$  photoreduction. *Green Chem. Eng.* **2022**, *3*, 157–164. [\[CrossRef\]](#)
22. Liu, G.; Wang, L.; Wang, B.; Zhu, X.; Yang, J.; Liu, P.; Zhu, W.; Chen, Z.; Xia, J. Synchronous activation of Ag nanoparticles and BiOBr for boosting solar-driven  $\text{CO}_2$  reduction. *Chin. Chem. Lett.* **2023**, *34*, 157–164. [\[CrossRef\]](#)
23. Wu, H.; Li, C.; Che, H.; Hu, H.; Hu, W.; Liu, C.; Ai, J.; Dong, H. Decoration of mesoporous  $\text{Co}_3\text{O}_4$  nanospheres assembled by monocystal nanodots on g- $\text{C}_3\text{N}_4$  to construct Z-scheme system for improving photocatalytic performance. *Appl. Surf. Sci.* **2018**, *440*, 308–319. [\[CrossRef\]](#)
24. Guo, S.; Zhao, S.; Wu, X.; Li, H.; Zhou, Y.; Zhu, C.; Yang, N.; Jiang, X.; Gao, J.; Bai, L.; et al. A  $\text{Co}_3\text{O}_4$ -CDots- $\text{C}_3\text{N}_4$  three component electrocatalyst design concept for efficient and tunable  $\text{CO}_2$  reduction to syngas. *Nat. Commun.* **2017**, *8*, 1828. [\[CrossRef\]](#) [\[PubMed\]](#)
25. Tian, J.; Zhong, K.; Zhu, X.; Yang, J.; Mo, Z.; Liu, J.; Dai, J.; She, Y.; Song, Y.; Li, H.; et al. Highly exposed active sites of Au nanoclusters for photocatalytic  $\text{CO}_2$  reduction. *Chem. Eng. J.* **2023**, *451*, 138392. [\[CrossRef\]](#)
26. Zhu, X.; Zhou, G.; Yi, J.; Ding, P.; Yang, J.; Zhong, K.; Song, Y.; Hua, Y.; Zhu, X.; Yuan, J.; et al. Accelerated Photoreduction of  $\text{CO}_2$  to CO over a Stable Heterostructure with a Seamless Interface. *ACS Appl. Mater. Interfaces* **2021**, *13*, 39523–39532. [\[CrossRef\]](#)
27. Si, J.; Xiao, S.; Wang, Y.; Zhu, L.; Xia, X.; Huang, Z.; Gao, Y. Sub-nanometer  $\text{Co}_3\text{O}_4$  clusters anchored on  $\text{TiO}_2(\text{B})$  nano-sheets: Pt replaceable Co-catalysts for  $\text{H}_2$  evolution. *Nanoscale* **2018**, *10*, 2596–2602. [\[CrossRef\]](#)
28. Zhu, X.; Yang, J.; Zhu, X.; Yuan, J.; Zhou, M.; She, X.; Yu, Q.; Song, Y.; She, Y.; Hua, Y.; et al. Exploring deep effects of atomic vacancies on activating  $\text{CO}_2$  photoreduction via rationally designing indium oxide photocatalysts. *Chem. Eng. J.* **2021**, *422*, 129888. [\[CrossRef\]](#)
29. She, X.; Xu, H.; Li, L.; Mo, Z.; Zhu, X.; Yu, Y.; Song, Y.; Wu, J.; Qian, J.; Yuan, S.; et al. Steering charge transfer for boosting photocatalytic  $\text{H}_2$  evolution: Integration of two-dimensional semiconductor superiorities and noble-metal-free Schottky junction effect. *Appl. Catal. B Environ.* **2019**, *245*, 477–485. [\[CrossRef\]](#)
30. Han, C.; Ge, L.; Chen, C.; Li, Y.; Xiao, X.; Zhang, Y.; Guo, L. Novel visible light induced  $\text{Co}_3\text{O}_4$ -g- $\text{C}_3\text{N}_4$  heterojunction photocatalysts for efficient degradation of methyl orange. *Appl. Catal. B Environ.* **2014**, *147*, 546–553. [\[CrossRef\]](#)
31. Cao, J.; Zhang, N.; Wang, S.; Zhang, H. Electronic structure-dependent formaldehyde gas sensing performance of the  $\text{In}_2\text{O}_3/\text{Co}_3\text{O}_4$  core/shell hierarchical heterostructure sensors. *J. Colloid Interface Sci.* **2020**, *577*, 19–28. [\[CrossRef\]](#) [\[PubMed\]](#)
32. Hu, L.; Zhang, G.; Liu, M.; Wang, Q.; Wang, P. Enhanced degradation of Bisphenol A (BPA) by peroxymonosulfate with  $\text{Co}_3\text{O}_4$ - $\text{Bi}_2\text{O}_3$  catalyst activation: Effects of pH, inorganic anions, and water matrix. *Chem. Eng. J.* **2018**, *338*, 300–310. [\[CrossRef\]](#)
33. Mo, Z.; Xu, H.; Chen, Z.; She, X.; Song, Y.; Lian, J.; Zhu, X.; Yan, P.; Lei, Y.; Yuan, S.; et al. Construction of  $\text{MnO}_2$ /Monolayer g- $\text{C}_3\text{N}_4$  with Mn vacancies for Z-scheme overall water splitting. *Appl. Catal. B Environ.* **2019**, *241*, 452–460. [\[CrossRef\]](#)
34. Zhu, X.; Liu, J.; Zhao, Z.; Yan, J.; Xu, Y.; Song, Y.; Ji, H.; Xu, H.; Li, H. Hydrothermal synthesis of mpg- $\text{C}_3\text{N}_4$  and  $\text{Bi}_2\text{WO}_6$  nest-like structure nanohybrids with enhanced visible light photocatalytic activities. *RSC Adv.* **2017**, *7*, 38682–38690. [\[CrossRef\]](#)
35. Jing, L.; Xu, Y.; Chen, Z.; He, M.; Xie, M.; Liu, J.; Xu, H.; Huang, S.; Li, H. Different Morphologies of  $\text{SnS}_2$  Supported on 2D g- $\text{C}_3\text{N}_4$  for Excellent and Stable Visible Light Photocatalytic Hydrogen Generation. *ACS Sustain. Chem. Eng.* **2018**, *6*, 5132–5141. [\[CrossRef\]](#)
36. She, X.; Wu, J.; Zhong, J.; Xu, H.; Yang, Y.; Vajtai, R.; Lou, J.; Liu, Y.; Du, D.; Li, H.; et al. Ajayan, Oxygenated monolayer carbon nitride for excellent photocatalytic hydrogen evolution and external quantum efficiency. *Nano Energy* **2016**, *27*, 138–146. [\[CrossRef\]](#)
37. Dong, G.; Zhang, Y.; Bi, Y. The synergistic effect of  $\text{Bi}_2\text{WO}_6$  nanoplates and  $\text{Co}_3\text{O}_4$  cocatalysts for enhanced photoelectrochemical properties. *J. Mater. Chem. A* **2017**, *5*, 20594–20597. [\[CrossRef\]](#)
38. Yang, J.; Zhu, X.; Yu, Q.; He, M.; Zhang, W.; Mo, Z.; Yuan, J.; She, Y.; Xu, H.; Li, H. Multidimensional  $\text{In}_2\text{O}_3/\text{In}_2\text{S}_3$  heterojunction with lattice distortion for  $\text{CO}_2$  photoconversion. *Chin. J. Catal.* **2022**, *43*, 1286–1294. [\[CrossRef\]](#)
39. Yang, J.; Zhu, X.; Mo, Z.; Yi, J.; Yan, J.; Deng, J.; Xu, Y.; She, Y.; Qian, J.; Xu, H.; et al. A multidimensional  $\text{In}_2\text{S}_3$ - $\text{CuInS}_2$  heterostructure for photocatalytic carbon dioxide reduction. *Inorg. Chem. Front.* **2018**, *5*, 3163–3169. [\[CrossRef\]](#)
40. Mo, Z.; Xu, H.; She, X.; Song, Y.; Yan, P.; Yi, J.; Zhu, X.; Lei, Y.; Yuan, S.; Li, H. Constructing Pd/2D- $\text{C}_3\text{N}_4$  composites for efficient photocatalytic  $\text{H}_2$  evolution through nonplasmon-induced bound electrons. *Appl. Surf. Sci.* **2019**, *467–468*, 151–157. [\[CrossRef\]](#)
41. Zhang, G.; Zhu, X.; Chen, D.; Li, N.; Xu, Q.; Li, H.; He, J.; Xu, H.; Lu, J. Hierarchical Z-scheme g- $\text{C}_3\text{N}_4$ /Au/ $\text{ZnIn}_2\text{S}_4$  photocatalyst for highly enhanced visible-light photocatalytic nitric oxide removal and carbon dioxide conversion. *Environ. Sci. Nano* **2020**, *7*, 676–687. [\[CrossRef\]](#)
42. Yan, P.; She, X.; Zhu, X.; Xu, L.; Qian, J.; Xia, J.; Zhang, J.; Xu, H.; Li, H.; Li, H. Efficient photocatalytic hydrogen evolution by engineering amino groups into ultrathin 2D graphitic carbon nitride. *Appl. Surf. Sci.* **2020**, *507*, 145085. [\[CrossRef\]](#)
43. Li, L.; Yi, J.; Zhu, X.; Zhou, M.; Zhang, S.; She, X.; Chen, Z.; Li, H.-M.; Xu, H. Nitriding Nickel-Based Cocatalyst: A Strategy To Maneuver Hydrogen Evolution Capacity for Enhanced Photocatalysis. *ACS Sustain. Chem. Eng.* **2019**, *8*, 884–892. [\[CrossRef\]](#)
44. Li, Q.; Zhu, X.; Yang, J.; Yu, Q.; Zhu, X.; Chu, J.; Du, Y.; Wang, C.; Hua, Y.; Li, H.; et al. Plasma treated  $\text{Bi}_2\text{WO}_6$  ultrathin nanosheets with oxygen vacancies for improved photocatalytic  $\text{CO}_2$  reduction. *Inorg. Chem. Front.* **2020**, *7*, 597–602. [\[CrossRef\]](#)
45. Feng, J.; Zhang, D.; Zhou, H.; Pi, M.; Wang, X.; Chen, S. Coupling P Nanostructures with P-Doped g- $\text{C}_3\text{N}_4$  As Efficient Visible Light Photocatalysts for  $\text{H}_2$  Evolution and RhB Degradation. *ACS Sustain. Chem. Eng.* **2018**, *6*, 6342–6349. [\[CrossRef\]](#)

46. Liu, G.; Liao, M.; Zhang, Z.; Wang, H.; Chen, D.; Feng, Y. Enhanced photodegradation performance of Rhodamine B with g-C<sub>3</sub>N<sub>4</sub> modified by carbon nanotubes. *Sep. Purif. Technol.* **2020**, *244*, 116618. [[CrossRef](#)]
47. Li, W.; Wang, Z.; Li, Y.; Ghasemi, J.B.; Li, J.; Zhang, G. Visible-NIR light-responsive 0D/2D CQDs/Sb<sub>2</sub>WO<sub>6</sub> nanosheets with enhanced photocatalytic degradation performance of RhB: Unveiling the dual roles of CQDs and mechanism study. *J. Hazard. Mater.* **2022**, *424*, 127595. [[CrossRef](#)] [[PubMed](#)]
48. Hu, Q.; Dong, J.; Chen, Y.; Yi, J.; Xia, J.; Yin, S.; Li, H. In-situ construction of bifunctional MIL-125(Ti)/BiOI reactive adsorbent/photocatalyst with enhanced removal efficiency of organic contaminants. *Appl. Surf. Sci.* **2022**, *583*, 152423. [[CrossRef](#)]
49. Nandigana, P.; Mahato, S.; Dhandapani, M.; Pradhan, B.; Subramanian, B.; Panda, S.K. Lyophilized tin-doped MoS<sub>2</sub> as an efficient photocatalyst for overall degradation of Rhodamine B dye. *J. Alloys Compd.* **2022**, *907*, 164470. [[CrossRef](#)]
50. Preetha, R.; Govinda raj, M.; Vijayakumar, E.; Narendran, M.G.; Varathan, E.; Neppolian, B.; Jeyapaul, U.; John Bosco, A. Promoting photocatalytic interaction of boron doped reduced graphene oxide supported BiFeO<sub>3</sub> nanocomposite for visible-light-induced organic pollutant degradation. *J. Alloys Compd.* **2022**, *904*, 164038. [[CrossRef](#)]
51. Chen, Y.; Su, X.; Ma, M.; Hou, Y.; Lu, C.; Wan, F.; Ma, Y.; Xu, Z.; Liu, Q.; Hao, M.; et al. One-dimensional magnetic flower-like CoFe<sub>2</sub>O<sub>4</sub>@Bi<sub>2</sub>WO<sub>6</sub>@BiOBr composites for visible-light catalytic degradation of Rhodamine B. *J. Alloys Compd.* **2022**, *929*, 167297. [[CrossRef](#)]
52. Naing, H.H.; Li, Y.; Ghasemi, J.B.; Wang, J.; Zhang, G. Enhanced visible-light-driven photocatalysis of in-situ reduced of bismuth on BiOCl nanosheets and montmorillonite loading: Synergistic effect and mechanism insight. *Chemosphere* **2022**, *304*, 135354. [[CrossRef](#)] [[PubMed](#)]
53. Li, C.; Zhao, Y.; Fan, J.; Hu, X.; Liu, E.; Yu, Q. Nanoarchitectonics of S-scheme 0D/2D SbVO<sub>4</sub>/g-C<sub>3</sub>N<sub>4</sub> photocatalyst for enhanced pollution degradation and H<sub>2</sub> generation. *J. Alloys Compd.* **2022**, *919*, 165752. [[CrossRef](#)]
54. Chen, Y.; Jiang, Y.; Chen, B.; Tang, H.; Li, L.; Ding, Y.; Duan, H.; Wu, D. Insights into the enhanced photocatalytic activity of O-g-C<sub>3</sub>N<sub>4</sub> coupled with SnO<sub>2</sub> composites under visible light irradiation. *J. Alloys Compd.* **2022**, *903*, 163739. [[CrossRef](#)]

**Disclaimer/Publisher's Note:** The statements, opinions and data contained in all publications are solely those of the individual author(s) and contributor(s) and not of MDPI and/or the editor(s). MDPI and/or the editor(s) disclaim responsibility for any injury to people or property resulting from any ideas, methods, instructions or products referred to in the content.